Citation: Sussmann, R. and Gierens, K.M., Differences in early contrail evolution of two-engine versus four-engine aircraft: Lidar measurements and numerical simulations, J. Geophys. Res., 106(D5), 4899-4911, 2001.

Differences in early contrail evolution of two-engine versus four-engine aircraft: Lidar measurements and numerical simulations

Ralf Sussmann
Fraunhofer-Institut für Atmosphärische Umweltforschung, IFU, Garmisch-Partenkirchen, Germany

Klaus M. Gierens
Deutsches Zentrum für Luft und Raumfahrt, DLR, Wessling, Germany

Abstract. Jet- and vortex-regime evolution of contrails behind cruising aircraft is investigated by focusing on the role of aircraft type. Cross-section measurements by ground-based lidar and observational analysis are combined with numerical simulations of fluid dynamics and microphysics in the wake of a two-engine aircraft. Depending on ambient humidity levels, contrail evolution behind short-/medium-range twin-turbofan airliners is classified into two scenarios, which is in contrast to the three scenarios observed for a wide-body four-turbofan aircraft. In the case of ice-subsaturated ambient air, a short visible contrail is formed behind a two-engine aircraft that disappears before the ice is fully entrained into the wingtip vortices (in most cases $\approx$ 4 s behind aircraft). The early evaporation of the ice is mainly due to the fast initial jet expansion, mixing the exhaust with the ambient air. Contrails behind a wide-body four-engine aircraft always survive at least until vortex breakdown (i.e., typically 2 min behind aircraft). This is simply due to the larger ice mass in the contrail because of the higher fuel flow rate. Generally, in the case of ice supersaturation, a diffuse secondary wake evolves above the primary vortex wake. For a two-engine aircraft, always the whole contrail persists, while for a four-engine aircraft, the ice inside the primary wake disappears in most cases after vortex breakdown, when the relative humidity is only slightly above ice saturation. In the more rare cases of higher ice-supersaturation the ice in the primary wake survives vortex breakdown and becomes part of the persistent contrail.

1. Introduction

The often observable phenomenon of contrail formation behind cruising aircraft [*Appleman*, 1953; *Schumann*, 1996] bears the potential to impact the regional radiation balance due to strongly increasing air traffic [*IPCC*, 1999]. In the vicinity of air corridors, often numerous individual contrails begin to overlap and form huge artificial cirrus decks. To model this process, it is crucial to understand the mechanisms determining the growth of individual contrails in the vertical and horizontal directions. Vertical extension is ruled by the dynamics of the downward trailing vortex pair that forms behind cruising aircraft ("vortex regime," $\approx$ 10–100 s behind aircraft). After vortex breakdown, horizontal growth is then determined by vertical shear of horizontal wind speed and turbulence in the "dispersion regime" [*Hoshizaki et al.*, 1975].

Previous studies on a four-engine aircraft have shown that the exhaust material behind each engine is entrained into the trailing vortices [*Miake-Lye et al.*, 1993; *Quackenbush et al.*, 1993; *Gerz and Ehret*, 1997]. Later, this material is partly detrained from the "primary wake," leaving back a vertical curtain of exhaust material ("secondary wake") above the downward traveling vortex pair. (Throughout this paper, "primary wake" means both the system of the two counterrotating wingtip vortices behind aircraft and the ice contained inside; "secondary wake" is the less ordered flow and ice above the primary wake). In our preceding work on vertical dispersion of four-engine aircraft contrails we performed the first experimental study of the secondary-wake phenomenon and reevaluated the hitherto postulated mechanisms of vortex-wake entrainment and detrainment of fluid [*Sussmann*, 1999]. We found an early detrainment (due to turbulence, shear forces, and baroclininc forces) starting as early as a few seconds behind aircraft and being present in all practical cases. Whether the detrained material then forms a visible secondary wake was conjectured to depend upon ambient humidity. In a subsequent work we thus investigated the role of ambient humidity for the evolution of four-engine aircraft contrails during the vortex phase [*Sussmann and Gierens*, 1999]. We found that considering wake dynamics plus microphysics is crucial for understanding the details of contrail evolution in the vortex phase; that is, we were able to explain the frequently observed phenomena of (1) a "vertical wake-gap" between the primary and the secondary wakes by local subsaturation at the upper stagnation point of the vortex system, and (2) the evaporation of the primary wake at the end of the vortex regime caused by adiabatic compression and heating within the downward traveling vortex system. Our previous research focused on a heavy four-engine (B747-type) aircraft.

In the case of a light two-engine aircraft, however, we find from lidar measurements and sky observations that the details

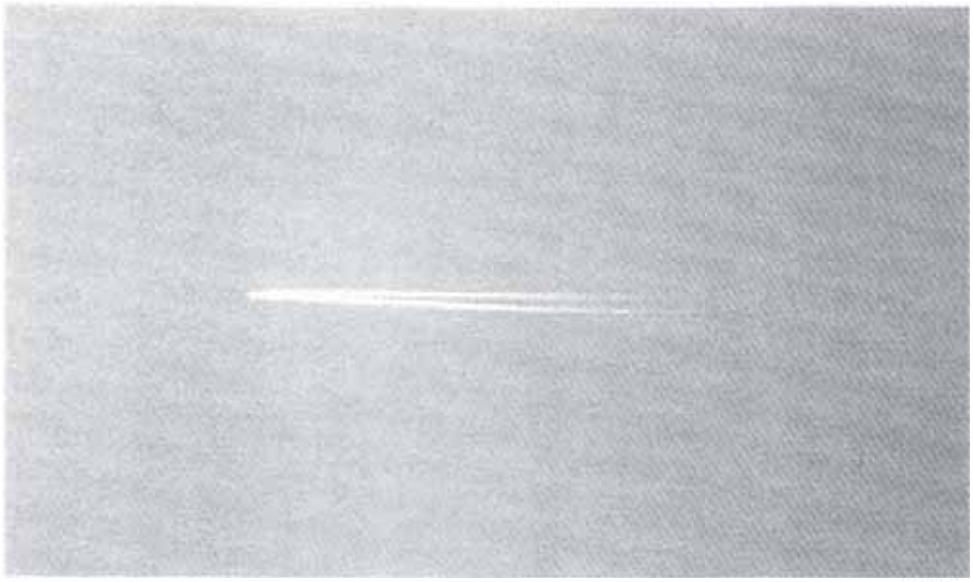

Figure 1. Photograph of a typical "short contrail," i.e., a quickly evaporating contrail observed behind a light two-engine aircraft.

of visible contrail evolution are different. For example, we often observe rather short contrails that are quickly evaporating and remain visible only up to typically 4 s (≈1 km) behind aircraft (Figure 1) but only for a small two-engine aircraft and never for a heavy four-engine aircraft. We found from our previous research that in the case of a wide-body four-engine aircraft, visible contrails always survive at least until vortex breakdown, i.e., ≈ 2 min behind aircraft [*Sussmann and Gierens*, 1999]. The goal of this paper is thus to understand the phenomenon of Figure 1 and, in general, to classify and understand all differences in the evolution of two-engine versus four-engine aircraft contrails. Thereafter, short-/medium-range two-turbofan airliners are denoted as "two-engine aircraft," whereas wide-body four-turbofan airliners are referred to as "four-engine aircraft."

In section 2 we present the various typical scenarios for the evolution of two-engine aircraft contrails as a function of ambient humidity as derived from empirical sky observations. These scenarios are compared with those of four-engine aircraft. The differences are briefly discussed in section 2.1. This is followed by a case study of a persistent contrail of a two-engine aircraft using ground-based lidar and CCD camera remote sensing (section 2.5). In section 3 we perform numerical simulations for two-engine aircraft contrails during the jet phase. Thereby we explain the observed evolution scenarios for two-engine aircraft contrails and their differences relative to four-engine aircraft. Section 4 is a summary of this work.

2. Observational Results

2.1. Empirical Contrail Scenarios Related to Ambient Humidity and Aircraft Type

We obtained statistics on typical possible scenarios in the vortex-regime evolution of contrails from eye observations of hundreds of aircraft at cruise conditions. In combination with each of the observations we investigated the occurrence of natural cirrus. This gives some rough indication on the ambient relative humidity levels with respect to ice (RH_i) in correlation with the observations. From these observations we define "empirical scenarios," i.e., two different scenarios for two-engine aircraft (Figure 2a) and three different ones for four-engine aircraft (Figure 2b, taken from *Sussmann and Gierens* [1999]). For all scenarios the Appleman criterion [*Appleman*, 1953; *Schumann*, 1996] is fulfilled.

2.2. Classification for Light Two-Engine Aircraft, Figure 2a

2.2.1. Scenario a1, about half of the observed cases. Two visible contrail tubes (jets) are formed and disappear again within the jet phase. This scenario is observed typically when nearly no features of natural cirrus are present ($RH_i < 100\%$). The major fraction of these contrails evaporate before about 4 s behind aircraft (≈ 1 km). In a small fraction of the observed cases, contrails survive up to the end of the vortex phase (≈ 2 min behind aircraft). See Figures 1 and 2a.

2.2.2. Scenario a2, about half of the observed cases. In the remaining fraction of all two-engine aircraft contrails, the contrails are persistent; that is, they remain visible significantly longer than the duration of the vortex phase. There appears a continuous vertical curtain of ice particles from the wingtip vortices up to the flight level (secondary wake). For a two-engine aircraft, always the whole contrail, i.e., primary plus secondary wakes, is persistent. This is usually observed in combination with formation of natural cirrus, i.e., $RH_i > 100\%$. See Figure 2a.

2.3. Classification for Heavy Four-Engine Aircraft, Figure 2b

Figure 2b shows the scenarios for a four-engine aircraft which have been investigated in detail in our previous work [*Sussmann and Gierens*, 1999]. Scenarios b1 and b2, respectively, are observed for about half of the observed cases. Scenario b3 is rarely observable mainly because situations with substantial supersaturation with respect to ice are much more seldom than slightly supersaturated ambient conditions [*Gierens et al.*, 1999]. Of course, contrails embedded within thick cirrus clouds are not observable.

Figure 2. (a) Two typical scenarios for the evolution of contrails of a light two-turbofan aircraft from observational analysis, correlated with the natural cirrus frequency of occurrence; (Scenario a1) nearly no cirrus ($RH_i < 100\%$); (a2) cirrus present ($RH_i > 100\%$). Each scenario occurs in about half of the observed two-engine cases. (b) Three typical scenarios for the evolution of contrails of a four-turbofan wide-body aircraft; (b1) nearly no cirrus ($RH_i < 100\%$); (b2) few cirrus ($RH_i > 100\%$ ^ $RH_i \sim 100\%$, "^" means "at the same time"); (b3) strong cirrus ($RH_i \gg 100\%$). Scenarios b1 and b2 occur in about half of the observed cases each, and scenario b3 is rarely observed.

2.4. Discussion of Differences

2.4.1. $RH_i < 100\%$. The difference between Scenarios a1 and b1 is that for a two-engine aircraft, the contrails disappear before typically 4 s (~ 1 km) behind aircraft (Scenario a1), while they survive always until the end of the vortex phase (age ~ 2 min) for a four-engine aircraft (Scenario b1).

Obviously, for subsaturated ambient air ($RH_i < 100\%$) the initially formed ice particles of the jets of a two-engine aircraft evaporate during the first ~ 4 s before being captured by the evolving vortices (Scenario a1). In the case of a four-engine aircraft, however, the ice from the jets can be entrained and thus be isolated from the dry ambient air before evaporating completely. The ice captured within the vortex pair remains visible until it is released after vortex breakdown. We suggest three possible mechanisms for an explanation of this difference: (1) different position of the engines: in the case of four-engine aircraft, at least one engine pair is placed farther outboard and thus close to the vortex cores, or (2) a stronger circulation of the vortices in the wake of heavier aircraft exerts a stronger attraction on the jets, or (3) higher fuel consumption leads to more ice on the jets which, as a consequence, needs more time to evaporate. Numerical simulations will address this question in detail in section 3.4.

2.4.2. $RH_i > 100\%$. In the case of a two-engine aircraft, only one scenario exists for $RH_i > 100\%$ (Scenario a2). Such a contrail does not show the two phenomena described and explained in our previous work for a four-engine aircraft, namely (1) a vertical wake-gap between the primary wake and the secondary wake and (2) the evaporation of the primary wake after vortex breakdown (Scenario b2 [*Sussmann and Gierens*, 1999]). We have already explained in our previous work that both phenomena are due to local subsaturation linked to the adiabatic heating within the down-traveling vortex pair. Both phenomena are not expected for a light (two-engine) aircraft where the downward motion is not fast enough for these phenomena to be developed [*Sussmann and Gierens*, 1999]. These two phenomena, typical for a four-engine aircraft, are suppressed only for substantial ambient humidities. Hence Scenario b3 appears similar to Scenario a2.

2.5. Measurement Case Study of Scenario a2

The measurements analyzed in this work were performed during the campaign CONTRAIL on April 23, 1996, near Augsburg, Germany. The research aircraft FALCON (18-m span twin-turbofan aircraft, for details see http://www.dlr.de/FB/OP/d-cmet_dat_d.html) produced a visible contrail at 1214 UT. Cross-section measurements of the contrail were performed by ground-based scanning lidar located at 48.3 °N, 10.7 °E, 500 m above sea level (asl). This measurement case study shows a typical two-engine aircraft contrail in Scenario a2 which may be compared to our previous case study on a B747 contrail, i.e., Scenario b2 [*Sussmann*, 1999].

2.6. Ambient Atmosphere

Data on the ambient atmosphere are obtained from in situ measurements onboard the FALCON. The visible contrail of the FALCON was formed at an altitude of 11425 m asl corresponding to a pressure of 217.2 hPa and a temperature of −62.5 °C. At flight level the Vaisala-Humicap sensor showed a relative humidity with respect to water of $RH_w = 62\%$ at the location of the lidar measurement (corresponding to a relative humidity with respect to ice of $RH_i = 111\%$). Stratification

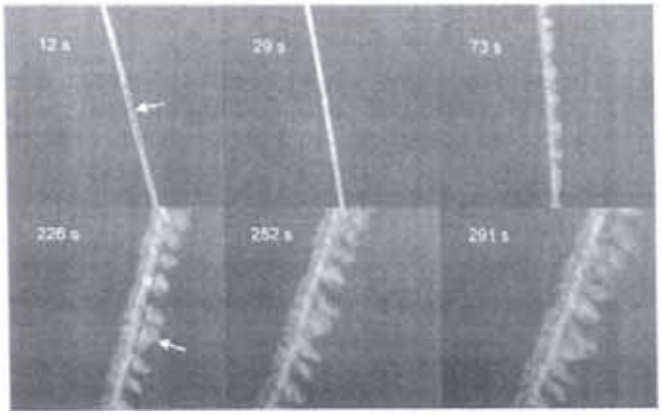

Figure 3. CCD image sequence of the vortex regime and dispersion regime evolution of a contrail of the research aircraft FALCON (between 12 and 291 s behind aircraft). Arrows indicate the starting points of the lidar to scan the cross sections shown in Plates 1a and 1b.

was moderate with a Brunt-Väisälä period of $N^{-1} = 76.2$ s (average for 11,165–11,425 m asl) derived from the vertical profile of potential temperature measured during the ascent/descent of the FALCON.

2.7. Ground-Based Lidar and CCD Camera Analysis

The instrumentation for ground-based remote sensing of contrails has been described in detail before [*Freudenthaler et al.*, 1994; *Sussmann*, 1999]. Briefly, we use a backscatter-depolarization lidar at 532 nm (52-cm-diameter Cassegrain telescope, Quanta-Ray GCR-4-10 laser). It is fixed on a computer-controlled angular scanning mount to track a contrail drifting with the wind. Contrail cross-sectional backscatter images are obtained from stepwise angular scanning and recording of lidar profiles (10 laser pulses each) and subsequent graphical interpolation of the lidar data. A CCD camera (Sony XC-77CE) is oriented parallel to the laser axis both for image sequencing of contrail evolution and for video guiding of the lidar angular scanning process.

2.7.1. CCD camera images. In Figure 3, a CCD image series of the FALCON contrail of the case study on April 23, 1996 (see above), is displayed between 12 and 291 s behind aircraft. At 12 s behind the FALCON, clearly the two vortex tubes marked by ice can be seen separately. The partial image at 29 s shows a phenomenon typical for contrails of two-engined aircraft: The two vortex tubes that were separated initially (at 12 s) are merged now (at 29 s); that is, they appear as one visible tube. This is never observed for four-engine aircraft contrails during the vortex phase, where the two vortex tubes remain separate until vortex breakdown [see *Sussmann and Gierens* [1999, Figures 3, 4, and 5]. Figure 3 shows at 73 s first signatures from vortex breakdown [*Crow*, 1970; *Chevalier*, 1973; *Spalart and Wray*, 1996]. Subsequently, between 226 and 291 s, strong mamma structures (i.e., hanging, breastlike protuberances on the undersurface of a cloud) evolve. It is obvious that even after vortex breakdown (i.e., after ≈ 73 s), there are structures (Crow rings) which still have a significant vorticity to travel farther down in the stratified atmosphere. While this has

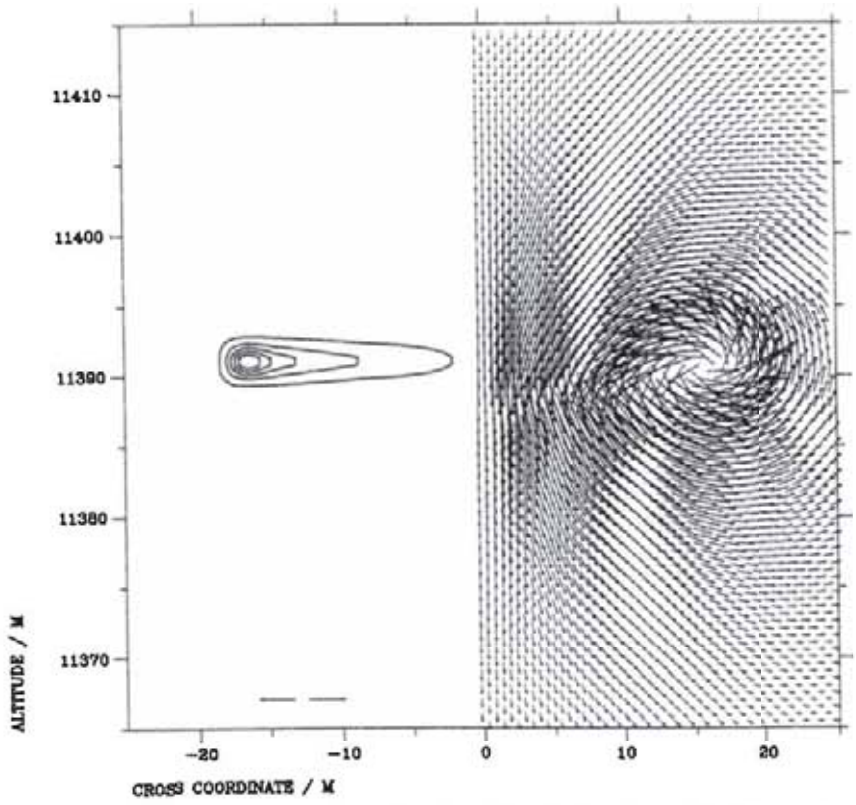

Figure 4. Initial flow field (vector arrows shown for the right wing) and vorticity (shown for the left wing) for an Airbus A320, as used for the initialization of the simulations. The aircraft wings are at the height of the centerline of the vorticity distribution. The two arrows in the left half of the figure represent a velocity of 5 m/s. Vorticity contour values are 1, 5, 10, 15, and 20 s^{-1}.

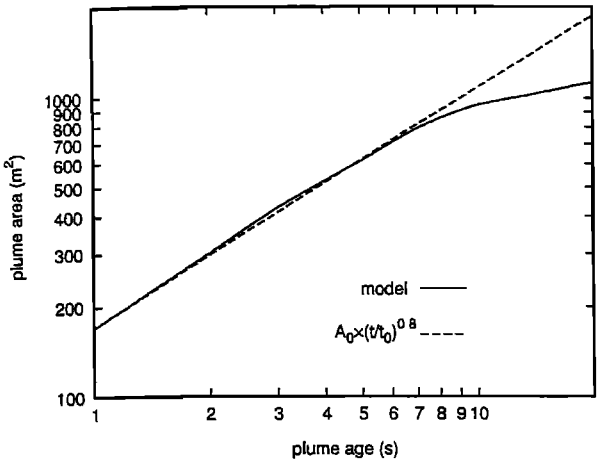

Figure 5. Plume area as a function of plume age for a model run with ice supersaturation everywhere, i.e., conserved total crystal number (solid line), and $t^{0.8}$ fit to many observations by *Schumann et al.* [1998]. The plume area is defined here as the area where $N_{ice}/\max(N_{ice}) > e^{-3}$. The modeled plume expansion initially follows almost exactly the $t^{0.8}$ law. Here t_0 is equal to 1 s, and the plume area at t_0 is A_0.

been discussed in principle in previous work [*Lewellen and Lewellen*, 1996; *Lewellen et al.*, 1998; *Gerz et al.*, 1998], the dominating quantitative aspect, i.e., the possibility that descending Crow rings can contribute to the major part of the total vertical extension of a visible contrail, has to our knowledge not yet been outlined. Although our case study might not be a typical case, it appears from the CCD image in Figure 3 together with the lidar measurements (compare Plates 1a and 1b below) that a significant portion of the vertical extension is present in the form of the mamma that evolved after Crow linking.

2.7.2. Lidar backscatter measurements. Vertical cross-sectional backscatter images perpendicular to the FALCON contrail are given in Plate 1. The lidar measurements for Plate 1a were recorded during a time span of 29–73 s behind the FALCON; that is, the plate displays a vortex phase image (see also Figure 3). Plate 1b was recorded for the same contrail during 249–291 s behind the FALCON, which is during the early dispersion phase (see also Figure 3). The maximum optical thickness derived from Plate 1b is 0.26, in the vertical direction. The optical thickness was retrieved from the lidar backscatter profiles using the shadow calibration technique [*Ruppersberg and Renger*, 1991]; for details, see *Sussmann* [1999].

Plate 1b shows a relatively high vertical extension of the contrail of 260 m; the lidar measurement shows a cross section through the center of one of the mamma structures (see also Figure 3). This extension is on the higher end of the vertical extensions, which are usually below 250 m. In our case this can be understood as being due to a relatively weak stratification of the ambient atmosphere (N^{-1} = 76.2 s; see above), which means only a weak hindrance of the downward motion of the vortex pair [*Greene*, 1986; *Schilling et al.*, 1996] and of the descending Crow rings later on, respectively. Furthermore, because of high ambient humidity levels (RH_w = 62%; see above), the commonly observed evaporation of the ice crystals in the lower part of the contrail due to the downward motion of the vortex pair [*Sussmann and Gierens*, 1999] does not occur. The contrail of Plate 1 and Figure 3 gives an example for Scenario a2 (Figure 2a).

2.7.3. Linear depolarization ratio. The linear depolarization ratio is defined as $\delta = I_\perp/I_{//}$, where the backscattered intensities, parallel polarized ($I_{//}$) and cross polarized ($I_\perp$) with respect to the laser field, are measured by two photomultipliers with perpendicular polarization orientations. Plate 1 (lower trace) displays the lidar-derived linear depolarization ratio in the same cross-sectional measurement domains as discussed above (Plate 1, upper trace). The depolarization ratio within the wake is in both measurement cases (lower trace of Plates 1a and 1b, respectively) close to the value of 0.5 found for natural cirrus [*Sassen*, 1991]. While for the dispersion regime measurement (Plate 1b, 247–291 s behind aircraft) this depolarization value is what we would have expected (i.e., aged persistent contrails being similar to natural cirrus), we have to discuss why we find this high value of 0.5 also for the early measurement shown in Plate 1a (29–73 s): In our previous work [*Sussmann*, 1999] we found from a measurement at comparable times, i.e., at ≈50 s behind a B747, a significantly smaller depolarization ratio of 0.35 within the vortex tubes (Plate 1b in the work of *Sussmann* [1999]). This was explained [*Sussmann*, 1999] in terms of the particles within the vortices being much smaller than the lidar wavelength (532 nm) or close to spherical [*Mishchenko and Travis*, 1994] due to the particles within the wingtip vortices being well isolated from the ambient atmosphere and thus being hindered in (non-spherical) crystal growth. We tentatively give two different reasons for this discrepancy to our new measurement behind the FALCON: (1) The lidar cross section measurement of Plate 1a failed in scanning the vortex cores and/or (2) the vortices behind the FALCON are weaker compared to the B747 case, thus the exhaust ice is not so strongly captured by the FALCON vortices and can more easily interact with the ambient air supersaturated with respect to ice, leading to a more rapid crystal growth even at this early stage (29–73 s).

3. Numerical Simulations

3.1. Model Setup for the Jet Phase

As in our previous paper [*Sussmann and Gierens*, 1999], we have used the hydrodynamics code MESOSCOP [*Schumann et al.*, 1987] to simulate the contrail and wake evolution. Because of the enormous requirements of computer time (small time steps, high resolution) and because we are not interested here in details of the crystal size spectra, the simulations have been performed with a bulk microphysics code that has already been used for other numerical contrail studies [*Gierens*, 1996; *Gierens and Ström*, 1998]. We assume here a lognormal ice crystal mass distribution. The only addition to this code relative to the earlier version is that we now have included the possibility of a decreasing number of ice crystals under sublimation conditions. This has been done in a simple way: If in a time step a fraction f of the ice mass in a certain grid box evaporates, a fraction f^x ($x > 1$) of the number density of ice crystals vanishes too. In this formulation both the mean crystal mass and the number of crystals decrease, which is realistic. If f is small (≈0), the ice mass decreases mainly by the shrinking of large crystals; if f is close to 1, the ice mass decreases mainly via the reduction of the crystal number. An exponent of x = 1.5 turned out to produce plausible results. (With an exponent of x = 2, the ice number density stays nearly constant until the ice mass vanishes almost completely; we feel this not to be

realistic.) Crystal growth and evaporation are the only microphysical processes of interest here. All simulations are two-dimensional (2-D) (span direction × height).

For the following process studies we use a rather simple ambient atmosphere with a constant lapse rate of 10 K/km (i.e., neutral stratification), ambient temperatures of about −61°C (cold cases) and −47 °C (warm cases), pressures about 220 hPa (cold) and 285 hPa (warm). We assume no wind, neither horizontal nor vertical, and no ambient turbulence. The relative humidity is used as a parameter that is varied from case to case.

The simulations have been performed in two steps: (1) computation of an initial flow field that refers to a very early stage in the jet phase (0.1 s plume age) and (2) simulation of the contrail evolution during the jet phase (typically up to a plume age of 10–20 s).

The first step was a necessary prerequisite for the jet phase simulations because it is unrealistic to simply assume a completely rolled-up vortex pair for this phase. Our initial flow field thus corresponds to a vortex sheet close to the wings that is just at the start of the roll-up process. We have computed this flow field as a superposition of many vortices along the wings, with an elliptical distribution of vorticity [*Ehret and Oertel*, 1994; *Gerz and Ehret*, 1997], such that the desired circulation around each wing (depending on the assumed aircraft weight, span, and speed) results. We prefer to make the simulations for the a more common aircraft, i.e., an Airbus A320, although our lidar case studies were performed only for the FALCON aircraft. (Differences in the position of the engines relative to the body of the aircraft turn out to have a minor influence on the contrail evolution from our numerical simulations below.) The initial vorticity distribution and velocity field for an Airbus A320 (weight = 600 kN, span = 34.10 m, speed = 840 km/h, circulation = 267 m^2/s) is shown in Figure 4.

We have placed a passive tracer into this flow field at the position of the jet engines. The initial tracer distribution was assumed to cover an area of 7 m^2 per jet (which is a few times larger than the engine exit area in order to account for the rapid spreading of the jet) and is assumed to have a truncated broad Gaussian shape. The thermal energy in the exhaust amounts to 79.1 kJ/m in the present case (assuming an overall propulsion efficiency of $\eta = 0.32$) and is distributed in the same way. The roll-up of the vortex sheet and the advection of the passive tracer are simulated at very high spatial and temporal resolution (200 × 200 grid points with 0.5 m × 0.5 m resolution and a time step of 0.01 s for the A320) up to a plume age of 0.1 s. The resulting fields are then smoothed to a coarser resolution of 1 m, whereas the inert tracer is replaced by ice crystals. For the A320, assuming a fuel flow of 0.314 kg/s, the mass of water vapor added to the plume per meter of flight path is 3.36 g, and assuming the emission of 10^{15} ice nuclei per kg fuel, the number of ice crystals is about 2.65×10^{12} m^{-1}. The thermal energy results in a maximum temperature anomaly in the jet of 19.1 K for the cold cases and 16.1 K for the warm cases at a plume age of 0.1 s.

Inside the jet we assume a strong turbulence caused by the friction between the ambient air and the jet, which leaves the engines with a velocity of about 200 m/s relative to the ambient air. Since the jet expansion cannot be mimicked in a 2-D model, the turbulent mixing of exhaust and ambient air has been modeled by setting the inverse Prandtl numbers, $1/Pr$ [see *Schumann et al.*, 1987, equation 27], for vapor and ice to a large initial value. Since the momentum of the jet is quickly distributed on more and more ambient air, the jet is decelerated. This has been modeled by decreasing $1/Pr$ exponentially with plume age t according to $1/Pr = 299 \times \exp(-t/5\text{s}) + 1$. The parameters of this empirical relation have been determined by trial and error until the modeled jet expansion followed the empirical $t^{0.8}$ law [*Schumann et al.*, 1998]. The strong initial jet turbulence is the origin of the rapid expansion of the jet and the fast mixing of the exhaust with ambient air. In Figure 5 we have plotted the plume area as a function of plume age, as it results from the described procedure. The plume area is defined as the area where the crystal number concentration is at least e^{-3} of the current maximum crystal concentration. For the determination of the area we have used a model run with ice supersaturation everywhere, so the total crystal number was conserved. It is seen from the figure that the initial jet expansion follows almost exactly the $t^{0.8}$ law, as determined from a multitude of plume measurements by *Schumann et al.*, [1998]. Possible deviations of this law during the first 0.3 s of plume age [*Schumann et al.*, 1999, Figure 1] could influence the nucleation of the ice which occurs on the same timescale. This does not affect our results since we have initialized our simulations assuming that the ice crystals are already nucleated. We have checked that an early deviation from the $t^{0.8}$ law has only a minor effect on the later contrail evolution.

Table 1. Overview Over Performed Simulations

RH_i, %	Grid Size, Spanwise × Height, m	Final Plume Age, s	Ambient Temperature, °C
12	100 × 100	5	−61
47	100 × 100	10	−61
74	100 × 100	15	−61
92	150 × 100	20	−61
99.5	150 × 100	20	−61
110	150 × 100	20	−61
87	100 × 100	10	−47
95	100 × 100	10	−47
111	100 × 100	10	−47

The simulations are sorted according to the ambient relative humidity with respect to ice, RH_i. The spatial resolution was 1 m, the time step 0.01 s.

3.2. Jet Phase Simulations, Cold Cases

We consider now young (jet phase) contrails in situations with different ambient relative humidities with respect to ice ranging from $RH_i = 12\%$ up to $RH_i = 110\%$. An overview over the performed simulations is given in Table 1. The initial ice mass in the plume is assumed to be composed of the water vapor released by the engines. This generally results in a non-equilibrium situation. However, after a few time steps the ice and vapor distributions relax to equilibrium: Where the total water concentration is below ice saturation, all ice evaporates, and where the total water concentration is above ice saturation, the ice evaporates until ice saturation is reached. Because of the initial Gaussian tracer distribution, ice at the rim of the jet evaporates completely in dry situations, whereas in the jet center, some of the ice remains after relaxation to equilibrium. The relaxation time is of the order 0.1 s. The initial flow field and ice mass distribution (IWC) at a plume age of 0.35 s is shown in Figure 6 for a case with $RH_i = 12\%$.

We start the discussion of the case studies with consideration of the driest simulated case with $RH_i = 12\%$. The rapid

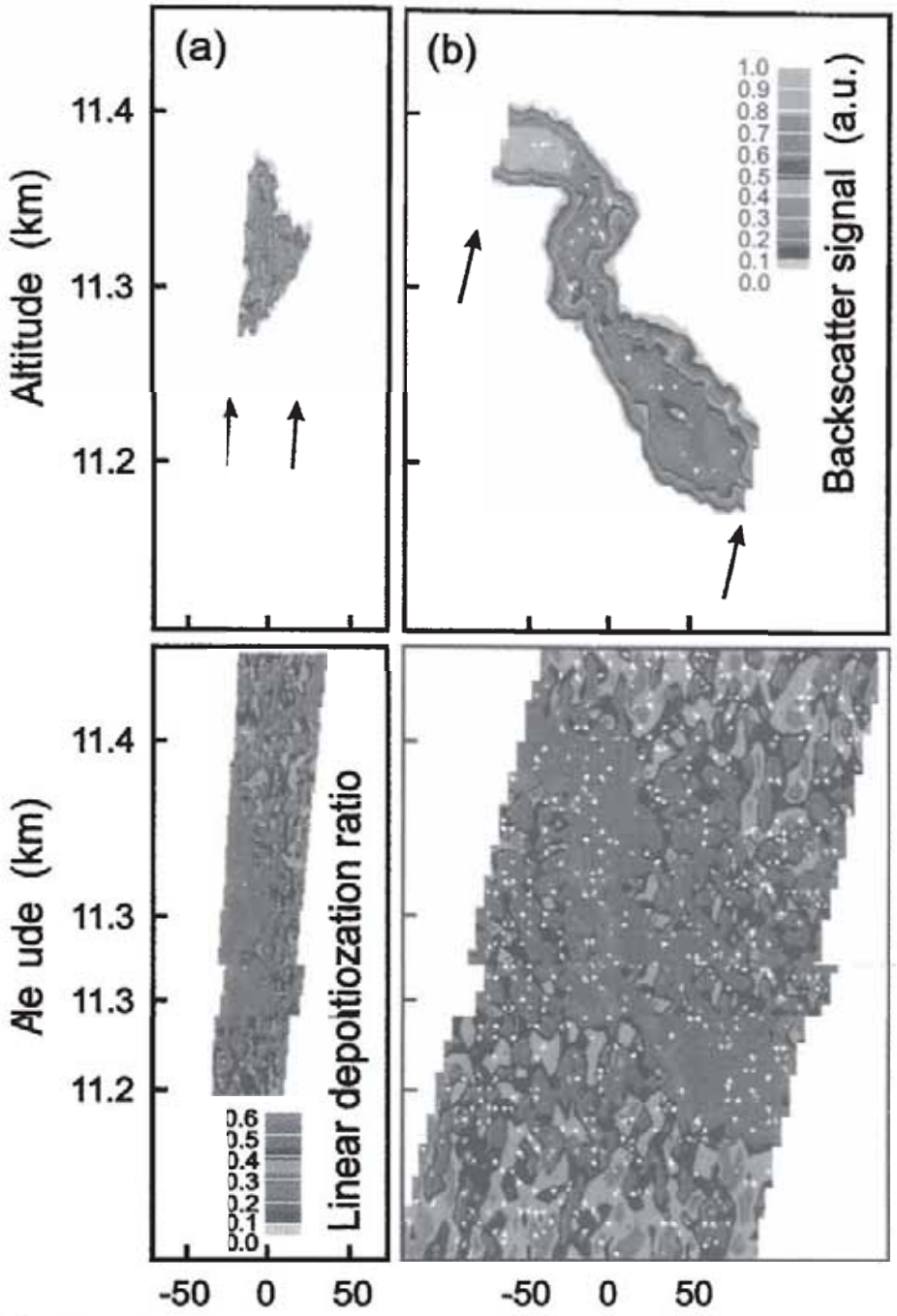

Plate 1. Ground-based lidar measurements of a contrail of the research aircraft FALCON. Color encoding gives the lidar backscatter signals within vertical cross sections perpendicular to the contrail. (a, top) Vortex-regime cross section recorded between 29 and 73 s behind aircraft. (b, top) Dispersion-regime cross section recorded between 247 and 291 s behind aircraft. (a, bottom) Cross sections as in the top trace, but the linear depolarization ratio is plotted. Arrows indicate the pointing of the scanning lidar.

mixing of the exhaust with such dry air leads to quick evaporation of the ice crystals and the contrail vanishes within 3–4 s from sight. The maximum optical thickness in the visual wavelength region becomes <0.1 at t = 2.25 s and <0.03 at t = 4 s. An extended object must have at least an optical thickness of 0.02 to be visible under excellent viewing conditions; how long a contrail remains visible from ground depends also on turbidity of the atmosphere and illumination of the contrail by the Sun. Under hazy conditions or with the Sun in the back (large scattering angles) the visibility threshold optical thickness can exceed 0.1. A photograph of a short contrail of a length less than 1 km was presented in Figure 1. It can be seen that the two ice trails move outward until they disappear. This means that the exhaust jets are still in the first quarter of a complete circle around the vortex cores when the contrail disappears. Exactly the same behavior is found in the simulation: The ice evaporates within the first quarter of the circle where it is pushed down by the strong downwash between the two vorti-

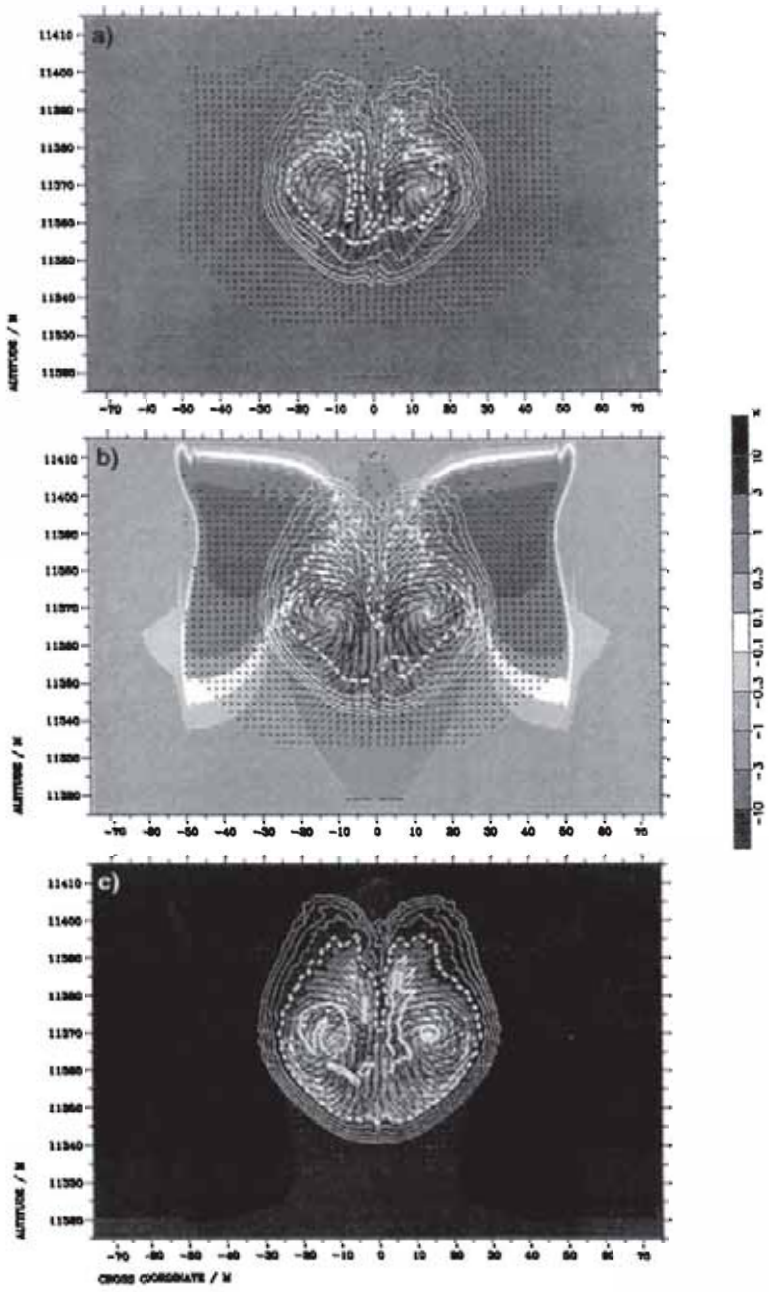

Plate 2. Velocity field (arrows), ice mass concentration (IWC, yellow contour lines), and ice supersaturation (color) for three A320 contrails at a plume age of 20 s and in situations with different relative humidity with respect to ice in the environment: (a) 92%, (b) 99.5%, and (c) 110%. The velocity field is nearly identical in all three cases; that is, there is not much influence on the dynamics by latent heat. The two arrows at the middle of the bottom line of each panel indicate a velocity of 5 m/s. The yellow IWC contours start with IWC = 0.01 mg/m^3 and increase with logarithmic steps of $10^{1/2}$. The thick dotted contour means IWC = 1 mg/m^3, and the thick solid line means IWC = 3 mg/m^3. The latter concentration is only reached in the case with RH_i = 110%. The color bar uses blue for subsaturation and red for supersaturation, again with logarithmic spacing. Plate 2b shows very clearly the influence of the vortex dynamics on the humidity field through adiabatic heating and cooling: where the downwash is strongest between the two vortices, there is strong subsaturation, whereas the upward motion at the outer rims of the two vortices leads to local supersaturation, which delays the evaporation of the ice crystals there. Even in a substantially supersaturated case as in Plate 2c the central downwash can lead to subsaturation and, consequently, to evaporation of ice.

ces. Adiabatic compression and heating aid in evaporation of the contrail. However, it must be emphasized that neither the adiabatic heating nor the mixing of the exhaust with ambient air due to the swirling motion alone would suffice for the quick evaporation of the contrail. As explained above, the jet expansion caused by the large backward momentum of the jet relative to the ambient air leads to quick mixing, in particular during the first few seconds. Indeed, the relative jet expansion

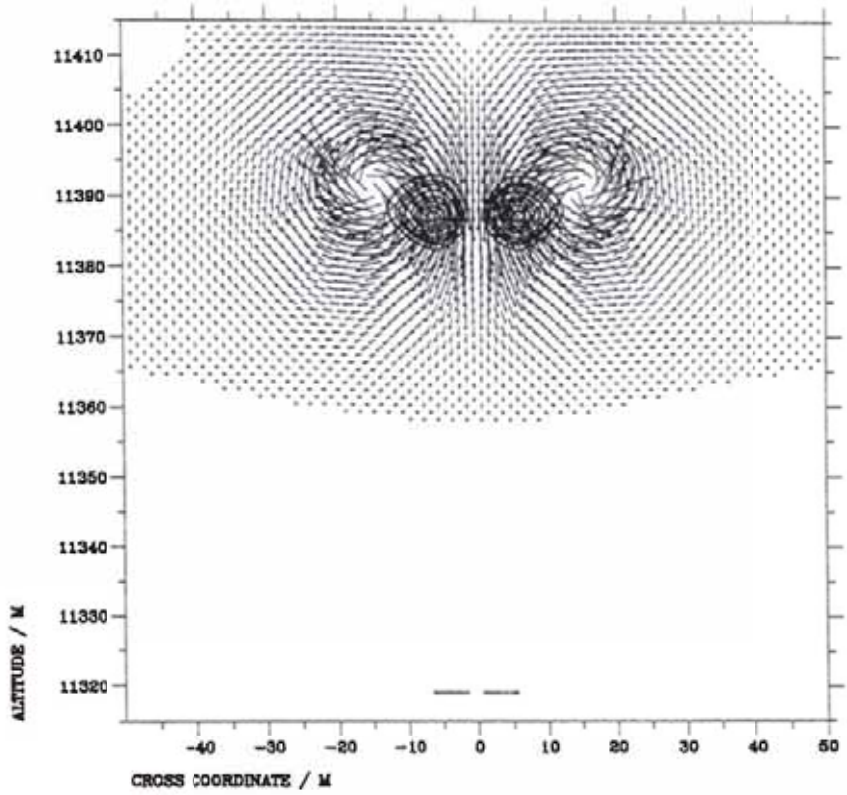

Figure 6. Flow field and ice mass concentration (IWC) at a plume age of 0.35 s for an Airbus A320. The lowest IWC contour level is 1 g/m^3, and the subsequent countour values are 3, 5, 10, 20, 30, 40, and 50 g/m^3. The two velocity vectors at the lower boundary of the domain represent 5 m/s.

rate ($d \ln A/dt$) $\propto t^{-1}$; that is, it is largest initially. Simulations without a modeled jet expansion (i.e., with unchanged inverse Prandtl numbers) did not succeed in reproduction of short contrails. Without this initial mixing the disappearance of the contrail would proceed much slower than observed.

It might be surprising that even in a much moister case with $RH_i = 47\%$, a contrail does not last much longer than in the drier case considered above. The maximum optical thickness falls below 0.1 at 4 s plume age and below 0.03 at 7.5 s plume age. A "mean" optical thickness (mean over the region where $\tau \geq 0.01$) falls below 0.03 at 6 s plume age. In an even moister case with $RH_i = 74\%$, the mean optical thickness sinks below 0.1 already at a plume age of 3.5 s and below 0.03 at a 14 s plume age. The corresponding maximum optical thickness reaches 0.1 at about 8.5 s. At the end of the simulation (15 s plume age) the maximum optical thickness is about 0.05 in this case. These results show that evaporating contrails of a two-engine aircraft are short and become invisible already during the jet phase for a rather wide variety of humidity conditions. In other words, we can well understand and simulate the observed empirical Scenario a1 (Figure 2a).

The results are summarized in Figure 7. It shows how steep the mean optical thicknesses of contrails decrease initially. The maximum optical thicknesses (not shown) display a similar behavior. Both evaporation of ice and its spatial dispersion by the jet expansion and the deformation of the jet by the vortices contribute to the decrease of the optical thickness of very young contrails. Thus the optical thickness decreases initially even in supersaturated cases. Contrails in environments with RH_i up to about 75% vanish from sight during the jet phase, i.e., within about 20 s plume age. The one considered contrail in supersaturated air is persistent and, of course, does not vanish at all. The remaining two contrails with $RH_i > 90\%$ evaporate slowly although the mean optical thickness is less than 0.1 at $t = 15$ s in the case with $RH_i = 92\%$, which can imply invisibility under unfavorable conditions. A simple theoretical consideration involving only the jet expansion (the $t^{0.8}$ law; see above and *Schumann et al.* [1998]) and assuming that all water substance exceeding ice saturation in the jet is actually ice gives the same qualitative result. This model yields an evaporation time, t_{evap}, at which the humidity in the jet

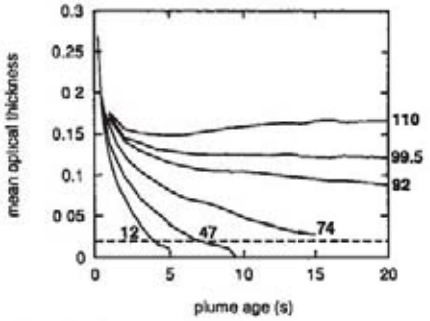

Figure 7. Simulated mean optical thickness of jet phase contrails as function of plume age. The ambient relative humidity with respect to ice is given at each curve. The dashed line is the visibility threshold under excellent viewing conditions for extended objects close to the observer, $\tau = 0.02$. Ambient temperature was −61 °C.

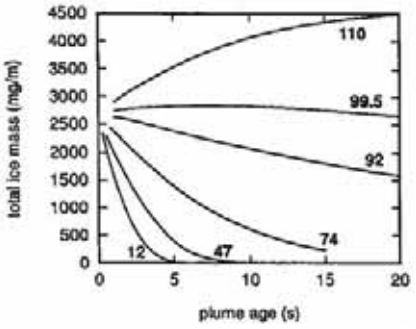

Figure 8. Simulated total ice mass per meter of flight path in jet phase contrails as a function of plume age. The ambient relative humidity with respect to ice is given at each curve. Ambient temperature was −61 °C.

changes from supersaturation to subsaturation. This is related to RH_i as follows: $t_{evap} \propto (100\% - RH_i)^{-1/0.8}$; that is, we find again that the contrail lifetime (which may be identified with t_{evap}) increases slowly for small values of RH_i and increases steeper and steeper as the humidity approaches saturation. These results are consistent with our observations of two-engine aircraft contrails, i.e., the empirical Scenarios a1 and a2 (Figure 2a).

The temporal evolution of total ice mass per meter of flight path is shown in Figure 8. These curves correspond to what has already been shown in Figure 7: There is quick evaporation of ice during the jet phase in cases with RH_i up to about 75% and much slower evaporation in the two subsaturated cases with $RH_i > 90\%$. In the supersaturated case, the ice mass is growing, as expected.

Let us discuss now in more detail the three simulations with high relative humidities with respect to ice of 92, 99.5, and 110%, respectively. These simulations were run up to a plume age of 20 s, and the domain has been extended in the spanwise coordinate to 150 m in order to minimize effects of the periodic lateral boundaries. Plate 2 shows the velocity field, the ice mass concentration, and the supersaturation field at the end of the three simulations, i.e., at $t = 20$ s. First, we note that the flow field is nearly identical in all cases, which means that the latent heat that is released or consumed because of the changing ice content hardly influences the dynamics. However, the dynamics does, in turn, influence the microphysics via adiabatic heating in the central downwash region and by adiabatic cooling near the upper outer rims of the two vortices. The latter is the location where background haze particles, if present, can freeze and add to the ice content of the contrail [*Gierens and Ström*, 1998]. The dynamic influence on the supersaturation field is most evident in the case with $RH_i = 99.5\%$ (Plate 2b); however, even in the other cases that have ambient humidities farther away from saturation, supersaturation can appear in a generally subsaturated environment (as indicated by the small reddish spot in panel 2a), and vice versa (the blue area in panel 2c). Indications of a development of a secondary wake can be seen in all three panels, although it is clear that such a curtain of ice must evaporate quickly in the two subsaturated cases, whereas it will be part of a persistent contrail later on in the supersaturated case. It can be seen in the figure that already at a plume age of 20 s the contrail extends to about a 10 m higher altitude in panel 2c with $RH_i = 110\%$ than in panel 2a with $RH_i = 92\%$. In the almost saturated case of panel 2b some ice can survive the vortex phase in the supersaturated "wings."

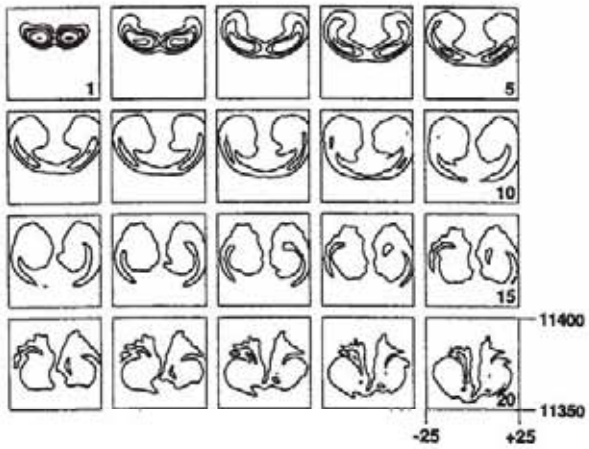

Figure 9. Time series of contrail cross sections during the jet phase, as simulated in a case with ambient relative humidity over ice of 92%. The plume age varies from 1 to 20 s from top left to bottom right and is indicated in some of the frames. The frame dimension is 50 m × 50 m. The plotted contours are ice mass concentrations of 1, 3, 5, 10, and 20 mg/m^3.

However, these wings will travel down with the vortex system, get weaker, and will vanish as soon as the vortex system collapses at the end of the vortex phase. This is one of the rare examples where a contrail of a two-engine aircraft will survive until the end of the vortex system.

Figure 9 shows a time series of contrail cross sections for the simulation with $RH_i = 92\%$. Shown are contours of ice mass concentration (ice water content (IWC)); the outermost contour represents IWC = 1 mg/m^3. In the first frame we see the two already expanded jets with a just beginning distortion due to the vortices. The maximum IWC is 21 mg/m^3, and the maximum number concentration of ice crystals is 2.5×10^4 cm^{-3}, which is a realistic value when compared to observational results presented by *Schröder et al.* [2000]. The subsequent frames show how the jets become rolled up around and into the vortices and how the IWC maxima vanish, which are present initially. At a plume age of 20 s the maximum values of both ice mass and crystal number concentrations is 1 order of magnitude smaller than initially, the maximum IWC is 2 mg/m^3, and the maximum number concentration is 2.3×10^3 cm^{-3}, again, consistent with the results of *Schröder et al.* [2000]. The moustache-like structure that the contrail obtains from $t = 2$s until about $t = 4$s has indeed been observed and photographed from a research aircraft during a hunt for contrails. The photograph is reproduced in Figure 10. Further-

Figure 10. Photograph of a very young contrail. Compare this photograph with the contrail cross section in frames 2–4 of Figure 9. (Photograph taken by U. Schumann.)

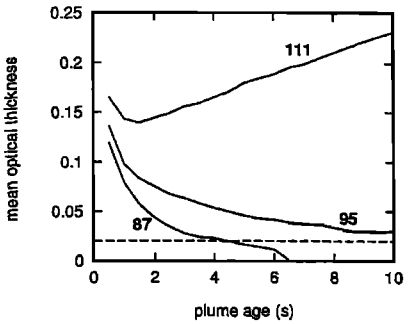

Figure 11. As Figure 7 but at −47 °C ambient temperature.

more, the figure shows that a ground observer would see only one single trail, especially when the contrail is not exactly in the zenith. This is consistent with many of our observations, see Figure 3 (29 s) for an example. In contrast, young contrails of a four-engine aircraft always show two distinct visible vortex tubes [see *Sussmann and Gierens*, 1999, Figures 3, 4, and 5].

3.3. Jet Phase Simulations, Warm Cases

We present now the results of three simulations where contrails have been assumed to form in an altitude of 9590 m asl at an ambient temperature of −47 °C and at a pressure of 285 hPa.

The relative contribution of emitted water to the total water in the plume is smaller in warmer air when the relative humidity is fixed. Therefore a contrail will disappear the faster the warmer the ambient air. Additionally, at the low temperatures of the upper troposphere where aircraft cruise, the diffusion of water vapor to and off ice crystals proceeds faster in warmer than in colder air [e.g., *Byers*, 1973, Figure 5.6]. Thus compared to the colder cases considered above, we expect that in the now discussed warmer cases, contrails will vanish faster in subsaturated conditions, while its ice crystals will grow faster under supersaturated conditions.

We have performed simulations at RH_i = 87, 95, and 111% up to a plume age of 10 s. The results are compiled in Figures 11 and 12. Figure 11 shows that in warm air a contrail vanishes already after 4–5 s at a relative humidity as high as 87% and that also, at the even higher relative humidity of 95% the contrail is at least rather faint after 5 s when its mean optical thickness falls below 0.05. Both the ice mass and the crystal number (not shown) of these two contrails decrease steadily right from the beginning. These results confirm our expectation that contrails are generally shorter at higher temperatures than at colder ones. A typical length of these contrails is 1–2 km.

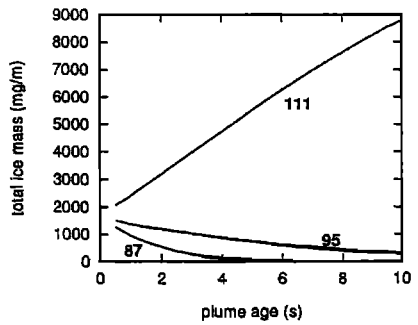

Figure 12. As Figure 8 but at −47 °C ambient temperature.

In the supersaturated case the optical thickness increases slowly after the initial decrease (which is caused by the downwash, as explained in the previous section). The increase of the optical thickness is due to the strongly growing ice mass (see Figure 12). The crystal number stays constant after an initial short phase of crystal loss due to evaporation in the downwash region. A cross section of this contrail at 10 s age is presented in Figure 13. It is seen that the ice mass concentration (IWC) exceeds 5 mg/m^3 in most of the vortex system, especially close to the two cores. The IWC is less only in the central downwash region and around the lower stagnation point of the vortex system. Much ice is still in the original flight altitude of 9590 m asl; this contrail will develop a continuous curtain of ice, i.e., a secondary wake, from the flight altitude down to the primary vortex system, while the latter descends down through the atmosphere.

3.4. Difference Between Jet Phase Contrails of Small and Large Aircraft

We have observed that contrails of a four-engine aircraft never disappear during the jet phase; under subsaturated conditions they always survive until the end of the vortex phase (Scenario b1, Figure 2b). In contrast, contrails of a two-engine aircraft can be very short and can disappear as early as a few seconds after exhaust (Scenario a1, Figure 2a). To find the reason for this difference, we have performed a couple of additional simulations, again, assuming an ambient temperature of −47 °C and a relative humidity of 87% with respect to ice.

First, we have checked the effect of engine position relative to the wingtips. The question is whether it is the closeness between the developing vortex cores and the outboard engines of a four-engine aircraft that is responsible for the survival of the contrail during the jet and vortex phases. For this, we simply doubled the distance between the engines and the fuselage of an A320. However, this measure alone did not lead to a longer contrail lifetime. Then we additionally multiplied all velocities with a factor of 2 (which is equivalent to assuming a doubled aircraft weight). This made it necessary to use a time step of 0.005 s. However, the resulting contrail was even shorter than in the corresponding A320 case of the previous section: after 4 s all the ice was evaporated. The reason for this is probably that the stronger swirl enhances considerably the mixing of exhaust and ambient air. Finally, we additionally took into account the higher fuel flow of big (four engines) aircraft and multiplied the initial ice mass and crystal number by 4, which resembles then the fuel flow of a B747. This experiment yielded a surviving contrail. Next, we turned off the swirl velocity doubling; that is, we used, again, the normal A320 flow field, in order to check whether the strong swirl (and thus the strong attractive power of the low pressure in the vortex cores) is essential for surviving contrails. The contrail lost its ice even slower in this case. This shows that of the two competing effects of stronger vortices, namely the confinement of the ice at the vortex cores which delays ice evaporation and on the other hand the enhanced mixing which accelerates ice evaporation, the latter is the more effective, at least under the circumstances that we have assumed for this test. Finally, we shifted the turbines back to their usual positions but kept the high fuel flow. Surprisingly, the result was nearly the same as with the turbines shifted outboard. Seemingly, the position of

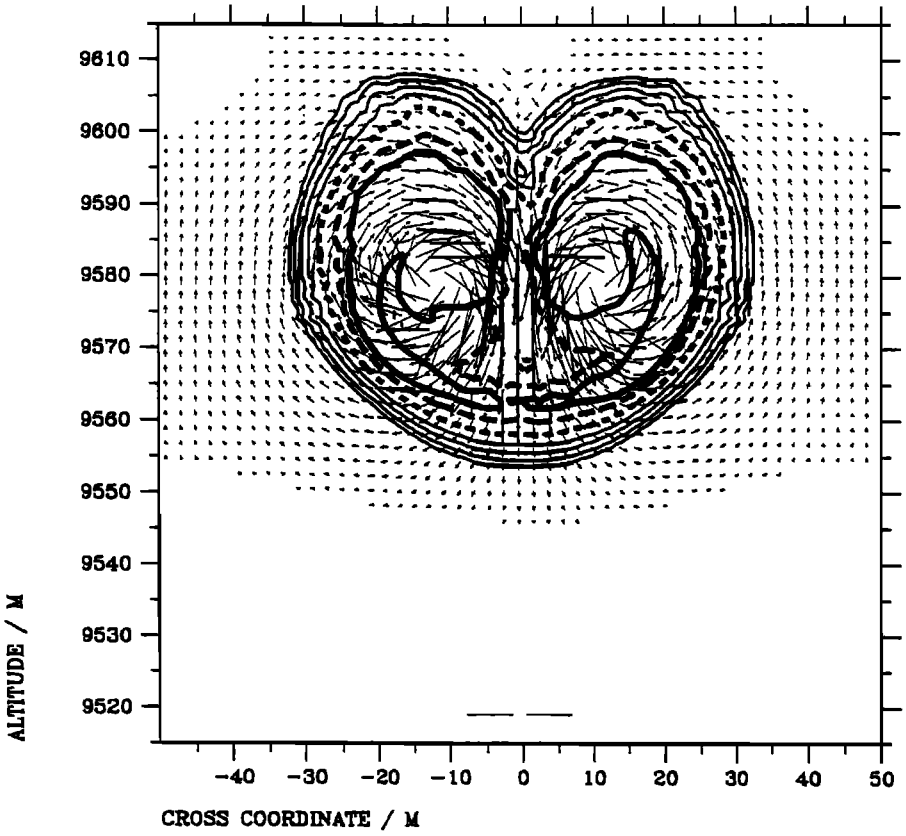

Figure 13. Flow field (arrows) and ice water content (IWC, contours) of a 10-s-old contrail in ambient air with $T = -47$ °C and $RH_i = 111\%$. The IWC contours are 0.01, 0.03, 0.1, and 0.3 mg/m^3 (thin lines), 1 mg/m^3 (thick dotted line), 3 mg/m^3 (thick dashed line), and 5 mg/m^3 (thick solid line). The two arrows at the bottom represent a flow speed of 5 m/s.

the engines relative to the wingtips has a negligible influence on contrail survival during the jet phase.

A comparison of the pseudo-"four-engine" contrails (i.e., the cases with increased fuel flow, double engine-fuselage distance, and doubled swirl velocity) and the A320 contrail of the previous section is presented in Figure 14, where the temporal evolution of total ice mass for these cases are plotted. It is seen that the ice mass loss rate is much smaller in the two pseudo-four-engine cases than in the two-engine case; the same holds for the crystal numbers (not shown). The ice mass loss rate is slower for normal than for double-swirl velocities as explained above. Obviously, the essential difference between small and big airliners is surprisingly an almost trivial one: It is mainly the fuel flow that matters; that is, in the case of big aircraft there is simply enough ice emitted into the plume so that a certain amount of the ice can survive the jet phase and is then closed up from the ambient air in the vortex system, until after about 2 min the vortices break up and these ice crystals are set free, mix with subsaturated ambient air, and evaporate.

4. Summary

In this paper we presented empirical sky observations and ground-based lidar studies of two-engine aircraft contrails. Thereby we formulated two scenarios for the contrail evolution of a two-engine aircraft as a function of ambient humidity. These were compared and contrasted to the three scenarios observed for a four-engine aircraft [*Sussmann and Gierens*, 1999]. We have performed the first numerical simulations of

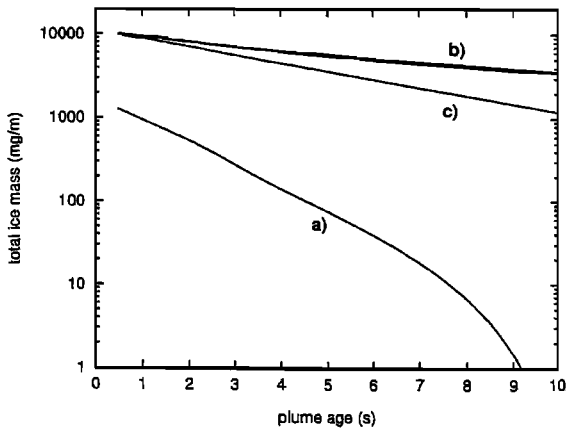

Figure 14. Total ice mass (mg/m) per meter of flight path versus plume age (s) for (a) the two-engine A320 of section 3.3. (b) Similar to Figure 14a but with doubled engine-fuselage distance and the fuel flow increased by a factor of 4. (c) Similar to Figure 14b but additionally with the swirl velocity doubled. Ambient conditions are $T = -47$ °C and $RH_i = 87\%$. The ice mass loss rate in Figures 14b and 14c is considerably smaller than that of the contrail of the true A320 (Figure 14a).

jet phase contrails, including their dynamics and microphysics, and were able to reproduce both two-engine aircraft contrail scenarios.

As a major finding, we identified the often observable short contrails (length ≈ 1 km) to be associated solely to a two-engine aircraft. The numerical simulations showed that it is the very fast jet expansion that is responsible for the quick mixing of the initially formed ice with subsaturated ambient air. This makes possible the fast evaporation of the ice within the jet phase. While most of the two-engine contrails in subsaturated air have only a length of ≈1 km, observations indicated that a smaller fraction survives up to the end of the vortex phase. The simulations showed, indeed, that the lifetime of the contrails depends in an exponential way on the ambient humidity: Only for high ambient humidities close to ice saturation, the lifetime becomes significantly longer than the typical 4 s. The lifetime also depends strongly on ambient temperature. Additionally, we checked possible mechanisms that make contrails of a four-engine aircraft always survive at least until the end of the vortex phase; that is, engine position close to the vortex cores and the magnitude of the vortex circulation alone cannot explain this. Rather, it was found to be simply due to the larger ice mass in the contrail of big (four engines) aircraft because of the higher fuel flow rate.

Acknowledgments. The authors would like to thank W. Seiler (IFU) and U. Schumann (DLR) for their continuous interest in this work. They are indebted to T. Gerz (DLR) for fruitful communications. Thanks to F. Homburg (IFU) who performed the measurements and to V. Freudenthaler (Universität München) for support in data handling. This research has been supported by the Commission of the European Union within "AEROCONTRAIL" of the Environment and Climate Program and in part by the German Bundesministerium für Bildung, Wissenschaft, Forschung und Technologie within the joint project "Schadstoffe in der Luftfahrt (Pollutants from Air Traffic)."

References

Appleman, H., The formation of exhaust condensation trails by jet aircraft, *Bull. Am. Meteorol. Soc.*, *34*, 14–20, 1953.

Byers, H. R., *Elements of Cloud Physics*, 191 pp., Univ. of Chicago Press, Chicago, Ill., 1973.

Chevalier, H., Flight test studies of the formation and dissipation of trailing vortices, *J. Aircraft*, *10*, 14–18, 1973.

Crow, S. C., Stability theory for a pair of trailing vortices, *AIAA J.*, *8*, 2172–2179, 1970.

Ehret, T., and H. Oertel, Numerical simulation of the dynamics and decay of trailing vortices including pollutants from air traffic, in *Impact of Emissions From Aircraft and Spacecraft Upon the Atmosphere*, edited by U. Schumann and D. Wurzel, pp. 268–273, Ger. Aerosp. Cent., Cologne, Germany, 1994.

Freudenthaler, V., H. Jäger, and F. Homburg, Ground-based mobile scanning lidar for remote sensing of contrails, *Ann. Geophys.*, *12*, 956–961, 1994.

Gerz, T., and T. Ehret, Wingtip vortices and exhaust jets during the jet regime of aircraft wakes, *Aerosp. Sci. Technol.*, *7*, 463–474, 1997.

Gerz, T., T. Dürbeck, and P. Konopka, Transport and effective diffusion of aircraft emissions, *J. Geophys. Res.*, *103*, 25,905–25,913, 1998.

Gierens, K. M., Numerical simulations of peristent contrails, *J. Atmos. Sci.*, *53*, 3333–3348, 1996.

Gierens, K. M., and J. Ström, A numerical study of aircraft wake induced ice cloud formation, *J. Atmos. Sci.*, *55*, 3253–3263, 1998.

Gierens, K. M., U. Schumann, M. Helten, H. G. J. Smit, and A. Marenco, A distribution law for relative humidity in the upper troposphere and lower stratosphere derived from three years of MOZAIC measurements, *Ann. Geophys.*, *17*, 1218–1226, 1999.

Greene, G. C., An approximate model of vortex decay in the atmosphere, *J. Aircraft*, *23*, 566–573, 1986.

Hoshizaki, H., L. B. Anderson, R. J. Conti, N. Farlow, J. W. Meyer, T. Overcamp, K. O. Redler, and V. Watson, Aircraft wake microscale phenomena, in *The Stratosphere Perturbed by Propulsion Effluents, CIAP, DOT-TST-75-53*, chap. 2, Natl. Tech. Inf. Serv., Springfield, Va., 1975.

Intergovernmental Panel on Climate Change (IPCC), *Aviation and the Global Atmosphere*, edited by J. E. Penner, D. H. Lister, D. J. Griggs, D. J. Dokken, and M. McFarland, 373 pp., Cambridge Univ. Press, New York, 1999.

Lewellen, D. C., and W. S. Lewellen, Large-eddy simulations of vortex-pair breakup in aircraft wakes, *AIAA J.*, *34*, 2337–2345, 1996.

Lewellen, D. C., et al., Large-eddy simulations and lidar measurements of vortex-pair breakup in aircraft wakes, *AIAA J.*, *8*, 1439–1445, 1998.

Miake-Lye, R. C., M. Martinez-Sanchez, R. C. Brown, and C. E. Kolb, Plume and wake dynamics, mixing, and chemistry behind a high-speed civil transport aircraft, *J. Aircraft*, *30*, 467–479, 1993.

Mishchenko, M. I., and L. D. Travis, Light scattering by polydispersions of randomly oriented spheroids with sizes comparable to wavelengths of observation, *Appl. Opt.*, *33*, 7206–7225, 1994.

Quackenbush, T. R., M. E. Teske, and A. J. Bilanin, Computation of wake/exhaust mixing downstream of advanced transport aircraft, *AIAA J.*, *93-2944*, 15, 1993.

Ruppersberg, G. H., and W. Renger, Invertierung der Lidarsignale von Cirrus und Kondensstreifen unter Nutzung des Schattenwurfes, *DLR Forschungsber. 91-07*, Dtsch. Forsch. und Versuchsanst. für Luft und Raumfahrt, Cologne, Germany, 1991.

Sassen, K., The polarization lidar technique for cloud research: A review and current assessment, *Bull. Am. Meteorol. Soc.*, *72*, 1848–1866, 1991.

Schilling, V., S. Siano, and D. Etling, Dispersion of aircraft emissions due to wake vortices in stratified shear flows: A two-dimensional numerical study, *J. Geophys. Res.*, *101*, 20,965–20,974, 1996.

Schröder, F., B. Kärcher, C. Duroure, J. Ström, A. Petzold, J.-F. Gayet, B. Strauss, P. Wendling, and S. Borrmann, On the transition of contrails into cirrus clouds, *J. Atmos. Sci.*, *57*, 464–480, 2000.

Schumann, U., On conditions for contrail formation from aircraft exhausts, *Meteorol. Z.*, *5*, 4–23, 1996.

Schumann, U., T. Hauf, H. Höller, H. Schmidt, and H. Volkert, A mesoscale model for simulation of turbulence, clouds and flow over mountains: Formulation and validation examples, *Beitr. Phys. Atmos.*, *61*, 413–446, 1987.

Schumann, U., H. Schlager, F. Arnold, R. Baumann, P. Haschberger, and O. Klemm, Dilution of aircraft exhaust plumes at cruise altitudes, *Atmos. Environ.*, *32*, 3097–3103, 1998.

Spalart, P. R., and A. A. Wray, Initiation of the Crow instability by atmospheric turbulence, in *The Characterisation and Modification of Wakes From Lifting Vehicles in Fluids*, pp. 18.1–18.8, Advis. Group for Aerosp. Res. and Dev., NATO, Brussels, 1996.

Sussmann, R., Vertical dispersion of an aircraft wake: Aerosol-lidar analysis of entrainment and detrainment in the vortex regime, *J. Geophys. Res.*, *104*, 2117–2129, 1999.

Sussmann, R., and K. Gierens, Lidar and numerical studies on the different evolution of vortex pair and secondary wake in young contrails, *J. Geophys. Res.*, *104*, 2131–2142, 1999.

K. M. Gierens, DLR, Institut für Physik der Atmosphäre, Postfach 1116, D-82230 Wessling, Germany. (klaus.gierens@dlr.de)

R. Sussmann, Fraunhofer-Institut für Atmosphärische Umweltforschung, Kreuzeckbahnstrasse 19, D-82467 Garmisch-Partenkirchen, Germany. (sussmann@ifu.fhg.de)

(Received April 7, 2000; revised July 5, 2000;
accepted August 19, 2000.)